

1 Dipole Pattern of Summer Ozone Pollution in the east of China and Its 2 Connection with Climate Variability

3 Xiaoqing Ma¹, Zhicong Yin¹²³

4 ¹Key Laboratory of Meteorological Disaster, Ministry of Education / Joint International Research Laboratory of
5 Climate and Environment Change (ILCEC) / Collaborative Innovation Center on Forecast and Evaluation of
6 Meteorological Disasters (CIC-FEMD), Nanjing University of Information Science & Technology, Nanjing
7 210044, China

8 ²Southern Marine Science and Engineering Guangdong Laboratory (Zhuhai), Zhuhai, China

9 ³Nansen-Zhu International Research Centre, Institute of Atmospheric Physics, Chinese Academy of Sciences,
10 Beijing, China

11 **Corresponding author:** Zhicong Yin (yinzhc@nuist.edu.cn)

12 **Address:** No. 219 Ningliu Road, Pukou District, Nanjing University of Information Science & Technology,
13 Nanjing 210044, China

14 **Tel.:** (+86) 136 5516 1661

15

16 **Abstract.**

17 Surface O₃ pollution has become one of the most severe air pollution problems in China, which makes it of
18 practical importance to understand O₃ variability. A south-north dipole pattern of summer-mean O₃ concentration
19 in the east of China (DP-O₃), which were centered at North China (NC) and the Pearl River Delta (PRD)
20 respectively, has been identified from the simulation of a global 3-D chemical transport model for the period
21 1980–2019. Large-scale anticyclonic (cyclonic) and cyclonic (anticyclonic) anomalies over NC and the PRD
22 resulted in a sharp contrast of meteorological conditions between the above two regions. The enhanced (restrained)
23 photochemistry in NC and restrained (enhanced) O₃ production in the PRD contributed to the DP-O₃. Decreased
24 sea ice anomalies near the Franz Josef Land and associated warm sea surface in May enhanced the Rossby-wave
25 source over northern Europe and West Siberia, which eventually induced an anomalous Eurasia-like pattern to
26 influence the formation of the DP-O₃. The thermodynamic signals of the southern Indian Ocean dipole were stored
27 in the subsurface and influenced spatial pattern of O₃ pollution in the east of China mainly through the Hadley
28 circulation. The physical mechanisms behind the modulation of the atmospheric circulations and related DP-O₃
29 by these two climate anomalies at different latitudes were evidently verified by large-scale ensemble simulations
30 of the earth system model.

31 **Key words:** ozone pollution; sea ice; Eurasia pattern; sea surface temperature; meridional circulation

32 1. Introduction

33 Surface O₃ is an important air pollutant. Exposure to high concentrations of O₃ is detrimental to both human
34 health and vegetation ecology (Rider and Carlsten, 2019). Since 2013, surface O₃ concentration has increased
35 over most parts of China, which is largely attributed to changes in anthropogenic emissions (Xu et al. 2018).
36 However, previous studies have shown that in addition to its trend of change, surface O₃ concentration also
37 demonstrated large interannual variations with significant regional differences (Zhou et al. 2013; Chen et al. 2019).
38 Based on analysis of 11 years of observational data over Hong Kong, Zhou et al. (2013) reported that the
39 interannual variation of O₃ concentration observed during 2000–2010 could reach up to 30% of the annual average
40 concentration. The O₃ concentration in Beijing also showed evident interannual variation during 2006–2016. For
41 example, the O₃ concentrations in the summers of 2012–2013 were lower by about 10 ppbv than that in 2011 and
42 2014 (Chen et al. 2019).

43 High O₃ events are usually associated with meteorological factors (e.g., intense solar radiation, high air
44 temperature and low humidity) favorable for O₃ formation, which can accelerate photochemical reaction and
45 weaken the dispersions and depositions (Han et al. 2020). For example, Lu et al. (2019) designed sensitivity
46 simulations to confirm that ozone pollution in China in 2017 was more serious than that in 2016, which was
47 attributed to the large enhancement of nature emissions of ozone precursors caused by hot and dry climate
48 condition in 2017. In the summer of 2013, the Yangtze River Delta experienced a severe heat wave with more
49 stagnant meteorological conditions. The upper-level anticyclonic circulation with sink airflows led to abnormally
50 low atmospheric water vapor content above the Yangtze River Delta and thus less than normal cloud cover, which
51 was conducive to a strong solar radiation environment and significant increases in surface ozone (Pu et al. 2017).
52 On the interannual to decadal time scale, anticyclonic anomalies over North China (NC) were critical for O₃
53 distribution in the summer and remotely linked with the effects of Eurasia teleconnection (EU) and west Pacific
54 patterns (Yin et al. 2019).

55 The Arctic sea ice (SI) declined rapidly while its variability has been increasing over the past decades, which
56 significantly affected summer atmospheric circulations over Eurasia (Lin and Li 2018). The preceding Arctic SI
57 anomalies could aggravate anomalously high air temperature and drought disasters in NC by triggering EU-like
58 atmospheric responses in summer (Wang and He 2015). Spring SI anomalies in the Barents Sea could prompt the
59 Silk Road Pattern and resulted in a north-south dipole pattern of summer air temperature anomalies in the east of
60 China (Li et al. 2021). When greater than normal SI occurred in the Barents Sea, local 500 hPa geopotential height
61 would decrease and a wave-chain would form, which subsequently induced more precipitation in the south of East

62 China but less precipitation in the north (Wang and Guo 2004). Sea surface temperature (SST) in the Pacific and
63 Indian oceans also have significant effects on atmospheric circulation over the east of China (Li and Xiao 2021;
64 Xia et al. 2021). SST anomalies in the South China Sea and the equatorial Eastern Indian Ocean could trigger the
65 East Asian - Pacific pattern and resulted in a dipole pattern of summer temperature and precipitation in the east
66 of China, i.e., areas to the north of the Yangtze River became cold and wet, while areas to the south were hot and
67 dry (Han and Zhang 2009; Li et al. 2018). Tian and Fan (2019) found that winter SST in the southern Indian
68 Ocean might affect spring-summer SST anomalies near Australia. In summer, the anomalous Hadley circulation
69 in the western North Pacific played an important role in summer precipitation over the middle and lower reaches
70 of the Yangtze River.

71 Although great attention in previous studies has been paid to the increase of ozone pollution, little is known
72 about changes in the spatial pattern of summer-mean O_3 in the east of China. As revealed by Yin and Ma (2020),
73 the dominant pattern of daily-varying ozone pollution in the east of China showed an interannual variation that
74 was mainly driven by the large-scale western Pacific subtropical high and the East Asian deep trough. For example,
75 the frequent movements of the western Pacific subtropical high and the East Asian deep trough both contributed
76 to the out-of-phase variations in O_3 over North China and the Yangtze River Delta (Zhao and Wang 2017; Yin
77 and Ma 2020). However, to the best of our knowledge, whether the north-south dipole pattern of the summer mean
78 O_3 pollution existed in the east of China still remains unclear. In this study, we attempted to explore the dominant
79 pattern of summertime O_3 in the east of China and associated physical mechanisms behind. Its connections with
80 preceding climate variability were also examined. The remainder of this paper was organized as follows. The data
81 and methods are described in Section 2. Section 3 examined the dipole pattern of summertime O_3 in the east of
82 China and its possible influencing factors. The associated physical mechanisms were studied in Section 4. Major
83 conclusions and discussion are provided in Section 5.

84 **2. Datasets and methods**

85 **2.1 Observations and Reanalysis Dataset**

86 Hourly ozone concentration observations from 2015 to 2019 were publicly available at
87 <https://quotsoft.net/air/> and the last accessible data were for 23 September 2020. The relevant data were detrended
88 before all computations were conducted for the study period.

89 The meteorological fields data with a horizontal resolution of 0.5° latitude by 0.625° longitude for the period
90 1980–2019 were taken from the MERRA-2 dataset (Gelaro et al., 2017), including geopotential height at 500 hPa

91 (Z500), surface incoming shortwave flux (Ssr), low and medium cloud cover (Mlcc), precipitation (Prec), 10-m
 92 zonal and meridional winds (UV10m), and surface air temperature (SAT) and zonal and meridional winds and
 93 vertical velocity at different vertical levels. Monthly Outgoing Longwave Radiation (OLR) data ($1^\circ \times 1^\circ$) could
 94 be acquired from the University of Maryland OLR Climate Data Record portal (<http://olr.umd.edu/>). Monthly SI
 95 concentrations and SST ($1^\circ \times 1^\circ$) for the period 1980 - 2019 were downloaded from the website of the Met Office
 96 Hadley Centre (Rayner et al. 2003). Monthly mean subsurface ocean temperatures in the upper 250 m with a
 97 horizontal resolution of $1^\circ \times 1^\circ$ were obtained from the Met Office Hadley Centre EN4 version 2.1 (Good et al.
 98 2013).

99 The wave activity flux (WAF) was computed to illustrate the propagation of Rossby wave activities (Takaya
 100 and Nakamura 2001):

$$101 \quad W = \frac{1}{2|\bar{U}|} \left[\bar{u}(\psi'^2_x - \psi'\psi'_{xx}) + \bar{v}(\psi'_x\psi'_y - \psi'\psi'_{xy}) \right]$$

$$102 \quad \left[\bar{u}(\psi'_x\psi'_y - \psi'\psi'_{xy}) + \bar{v}(\psi'^2_y - \psi'\psi'_{yy}) \right]$$

102 where subscripts denote partial derivatives; the overbar and prime represent the climatological mean and
 103 anomaly, respectively; ψ' represents the stream function anomaly. U is the horizontal wind speed; u and v are the
 104 zonal and meridional wind components, respectively; and W denotes the two-dimensional Rossby WAF. The
 105 Rossby wave source $-\nabla \cdot V_\chi(f + \xi)$ proposed by Sardeshmukh and Hoskins (1988) is also calculated in this
 106 study. V , ξ and f refer to the horizontal wind velocity, relative vorticity and geostrophic parameter,
 107 respectively. ∇ is horizontal gradient; subscript χ represents divergent component.

108 2.2 1980–2019 O₃ concentrations simulated by GEOS-Chem

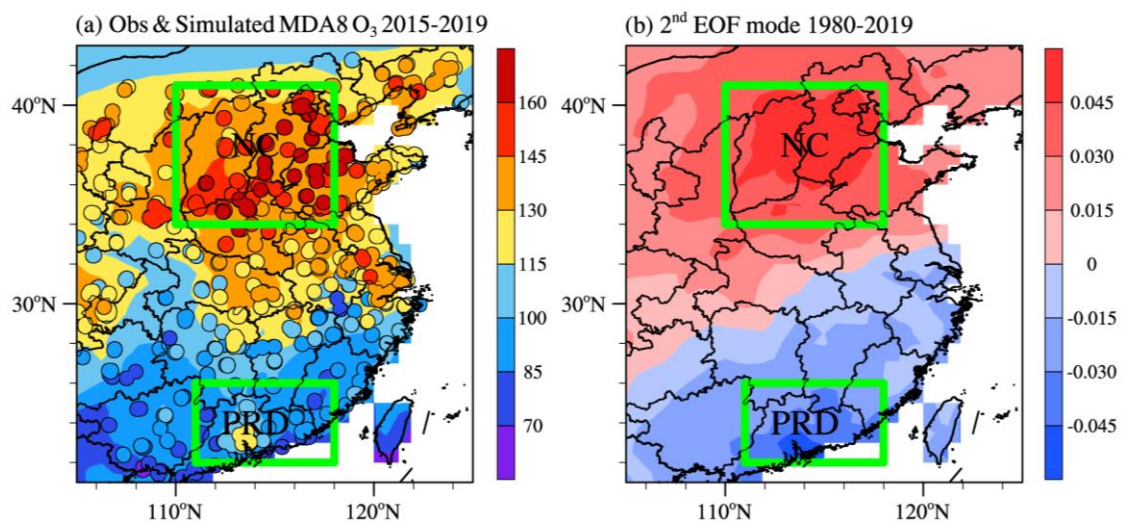
109 Hourly ozone concentrations were simulated by the nested-grid version of the global 3-D chemical transport
 110 model (GEOS-Chem), which included detailed description of oxidant–aerosol chemistry. The model was driven
 111 by MERRA-2 assimilated meteorological data (Gelaro et al. 2017). The nested grid over China ($15\text{--}55^\circ\text{N}$, 75--
 112 135°E) had a horizontal resolution of 0.5° latitude by 0.625° longitude and consisted of 47 vertical layers up to
 113 0.01 hPa. The GEOS-Chem model included the fully coupled O₃–NO_x–hydrocarbon and aerosol chemistry
 114 modules with more than 80 species and 300 reactions (Bey et al. 2001).

115 Chemical and physical processes were examined using the outputs of GEOS-Chem. Because non-local
 116 planetary boundary layer (PBL) mixing was used, emissions and dry deposition trends within the PBL were
 117 applied within the mixing (Holtslag and Boville, 1993). Compared with other terms, the value of wet deposition
 118 was extremely small, so it was not considered in this study (Liao et al., 2006). Consequently, the major chemical
 119 and physical processes related to meteorological conditions included the chemistry, convection, PBL mixing,

120 transport and their sum within the PBL were the focus.

121 The GEOS-Chem model has been widely used to examine historical O₃ changes in China. Yang et al. (2014)
122 evaluated the simulated interannual variation of June–July–August (JJA) surface-layer O₃ concentration at the
123 Hok Tsui station (22°13'N, 114°15'E). They found that the model could well capture the peaks and troughs of the
124 observed JJA O₃ concentration with a high correlation coefficient of +0.87 (exceed the 99% confidence level)
125 between simulations and observations. Moreover, the model could also realistically simulate the spatial
126 distribution of O₃, and the spatial correlation coefficient between simulations and observations in the summer of
127 2017 could reach up to 0.89 (Li et al. 2019). These studies indicated that the GEOS-Chem model could capture
128 the interannual variation and distribution of the surface O₃ concentration fairly well.

129 The GEOS-Chem model successfully reproduced the dominant patterns of summer O₃ pollution on a daily
130 scale from 2015 to 2019 (Yin and Ma 2020). In this study, we first simulated the maximum daily average 8 h
131 concentration of O₃ (MDA8 O₃) from 2015 to 2019 and evaluated the performance of GEOS-Chem. The simulated
132 spatial distribution of MDA8 O₃ was similar to that of observations with a spatial correlation coefficient of 0.87
133 (Fig. 1a). Compared the simulated and observed summer mean MDA8 O₃ concentrations in NC and the PRD,
134 which had a low bias with a mean absolute error of 5.7 μg m⁻³ and 12.1 μg m⁻³ in the PRD and NC, respectively.
135 The values of root mean square error / mean were 15.8 % and 8.1 % in NC and the PRD, respectively. The observed
136 and simulated summer MDA8 O₃ anomalies in the east of China also presented consistent interannual differences
137 (Fig. S1a, b). The high consistency in both the temporal and spatial distributions between the simulations and
138 observations provided a solid evidence to support the feasibility of the present study.



139

140 **Figure 1** (a) Spatial distributions of observed (dots) and GEOS-Chem simulated (shading) summer-mean MDA8 O₃ (unit: μg
141 m⁻³) for the period 2015–2019. (b) The second EOF spatial pattern of simulated summer-mean MDA8 O₃ from 1980 to 2019.

142 The simulated O₃ concentrations were produced by GEOS-Chem with fixed emissions but changing meteorological conditions
143 from 1980 to 2019. The green boxes represent the areas of NC and the PRD.

144 Based the above results, the GEOS-Chem model was then driven by fixed anthropogenic and natural
145 emissions in 2010 and changing meteorological fields from 1980 to 2019 to highlight the impact of climate
146 variability on O₃ concentration. Results of this simulation were analyzed to reveal the dominant pattern of ozone
147 pollution in the east of China in summer and its relationship with preceding climate anomalies.

148 **2.3 Numerical experiments with CESM-LE**

149 To provide evidences that support the proposed connections between SI and SST and large-scale atmospheric
150 circulations, the simulations of the Community Earth System Model Large Ensemble (CESM-LE) were employed
151 (Kay et al. 2015). The CESM consists of coupled atmosphere, ocean, land, and sea ice component models. The
152 40-member ensemble of CESM-LE simulations over the period (1980–2019) includes a historical simulation
153 (1980–2005) and a representative concentration pathway (RCP) 8.5 forcing simulation (2006–2019). To confirm
154 the impact of preceding climate variability and associated physical mechanisms, composite analyses were
155 conducted based on the three years with the lowest and highest simulated preceding climatic variability for a
156 particular month in each member. The composite results of atmospheric circulations could be considered as the
157 relevant atmospheric responses associated with the preceding climate variability.

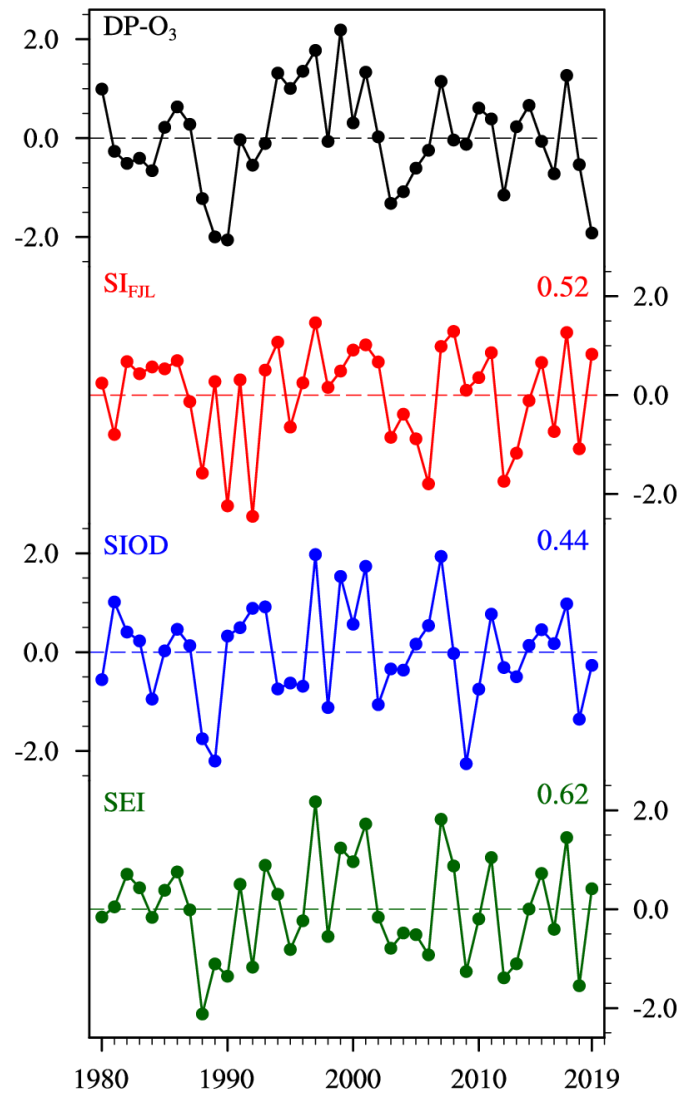
158 **3. Dipole pattern of summer O₃ and possible influencing factors**

159 As aforementioned, the GEOS-Chem model has a good performance in simulating O₃ concentration. The
160 summer O₃ concentrations from 1980 to 2019 was simulated by GEOS-Chem, and the EOF approach was applied
161 to the GEOS-Chem simulation to explore the dominant patterns of summer mean O₃ pollution in the east of China.
162 Percentage contributions to the total variance by the first and second EOF modes were 39% and 17.5%,
163 respectively. The significance test of the EOF eigenvalues confirmed that the first and second patterns were
164 distinctly separated (passing the North test, North et al, 1982). The first EOF pattern displayed a monopole pattern
165 (Fig. S2). The second EOF pattern presented a north-south dipole pattern of O₃ (DP-O₃) distribution in the east of
166 China with the two centers located in NC and the Pearl River Delta (PRD, Fig. 1b), respectively. Observations
167 have shown that high O₃ concentration frequently occurs in NC, and O₃ pollution in the PRD has become
168 increasingly serious in recent years (Liu et al. 2020). Furthermore, about 80% of the MDA8 O₃ anomalies in NC
169 were in opposite sign to those in PRD during 2015–2019 (Fig. S1a, b). Therefore, despite the fact that it was only
170 the second leading EOF mode, we still focused on the investigation of DP-O₃ in the present study, since it was
171 more similar to the actual pollution situation. Impacts of climate variability are also analyzed.

172 The MDA8 O₃ anomalies were divided into positive (P) and negative phases (N) of DP-O₃ (Fig. S3). For
173 convenience, DP-O₃P and DP-O₃N were defined by the EOF time series of DP-O₃ greater than 1 standard
174 deviation and less than $-1 \times$ standard deviation, respectively. The DP-O₃P corresponded to positive anomalies of
175 MDA8 O₃ in the north and negative anomalies in the PRD (Fig. S3a). In contrast, high concentration of O₃
176 occurred in the PRD and low concentration center appeared in NC under the DP-O₃N condition (Fig. S3b). The
177 correlation coefficient between time series of DP-O₃ and MDA8 O₃ difference between NC and the PRD was 0.91,
178 indicating that DP-O₃ reflected the opposite changes of O₃ concentration in NC and the PRD.

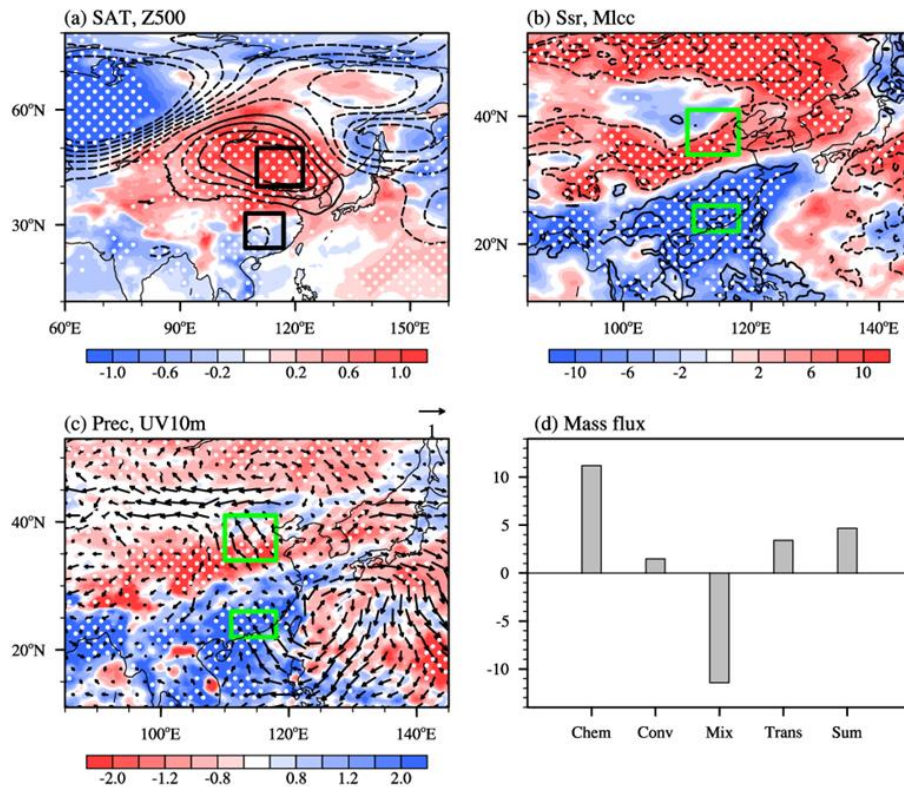
179 With fixed emissions, the changes in O₃ concentrations from 1980 to 2019 were solely caused by
180 meteorological conditions. The time series of DP-O₃ showed a strong interannual variation (Fig. 2). Composite
181 differences in large-scale atmospheric circulation and meteorological condition related to DP-O₃ between the
182 positive and negative phases (DP-O₃P minus DP-O₃N) were analyzed to explore the impacts of atmospheric
183 circulation on photochemical reactions and accumulations of various pollutants in the above two areas. During
184 the positive phase of DP-O₃, cyclonic and anticyclonic anomalies in the middle troposphere were found over the
185 PRD and NC (C_{PRD} and AC_{NC}) (Fig. 3a), respectively. The C_{PRD} and accompanied southerly winds in the PRD
186 efficiently transported clean and moist air from the sea to the PRD (Fig. 3c). Furthermore, low and medium cloud
187 covers were significantly increased, which led to weak solar radiation and reduced photochemical reactions (Fig.
188 3b). A moist, cool environment and weak solar radiation were conducive to low O₃ concentration in the PRD. On
189 the other hand, the positive anomalies of geopotential height in NC increased surface air temperature (Fig. 3a),
190 resulting in a dry environment with decreased cloud covers and sunny weather (Fig. 3b, c).

191 In order to provide a more quantitative evaluation of the contribution of chemical and physical processes, in
192 Fig. 3d, we examine the area-averaged differences in O₃ changes for NC and PRD. Chemistry represents the
193 changes in net chemical production, which appears to be the dominating process, leading to the greatest O₃ change
194 between NC and the PRD (12.3 Tons d⁻¹, Fig. 3d). Transport represents the change in horizontal and vertical
195 advection of ozone. Depending on the ozone concentration gradient and wind anomalies, the transport difference
196 between NC and PRD is 3.1 Tons d⁻¹ (Fig. 3d). Convection changes slightly in NC and PRD. As the mixing
197 process transports ozone along the vertical concentration gradient, it generally contributes negatively to the total
198 ozone change. The above analysis indicates that different meteorological conditions between NC and the PRD led
199 to the difference of O₃ concentration in the two regions (differed by 5.2 Tons d⁻¹), which eventually contributed
200 the formation of DP-O₃.



201

202 **Figure 2** Variations in standardized DP-O₃ time series (black), May SI near the Franz Josef Land (SI_{FJL}, red), January–
 203 February–March mean Subtropical Indian Ocean Dipole (SIOD, blue), and SEI (green) from 1980 to 2019. SEI defined as the
 204 weighted average of SI_{FJL} and SIOD. The correlation coefficients of the DP-O₃ with SI_{FJL} (red), SIOD (blue), and SEI (green)
 205 were shown in the figure.

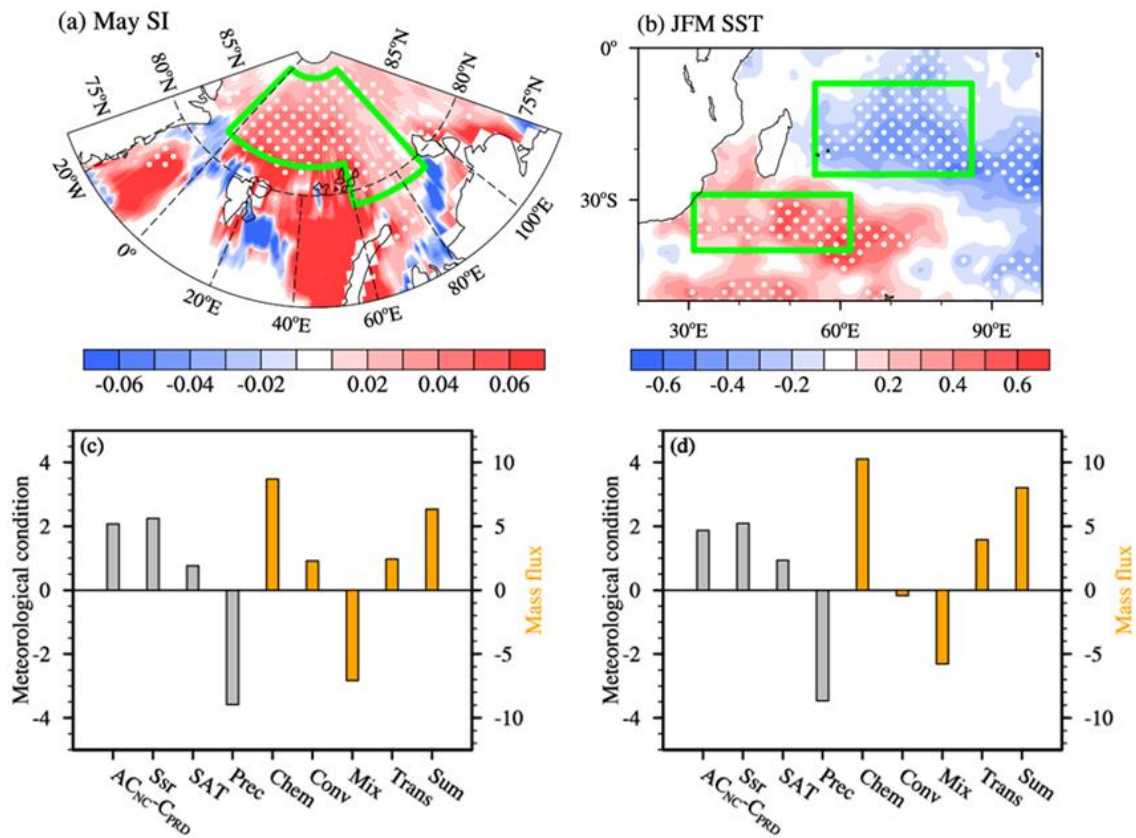


206

207 **Figure 3** Composite summer atmospheric circulations associated with the DP-O₃ (DP-O₃P minus DP-O₃N) for the period 1980
 208 to 2019, including (a) surface air temperature (SAT, unit: K, shadings) and geopotential height at 500 hPa (unit: 10 gpm,
 209 contours), (b) surface incoming shortwave flux (Ssr, unit: W m⁻², shadings) and low and medium cloud cover (Mlcc, unit: 1,
 210 contours), and (c) precipitation (Prec, unit: mm, shadings) and surface wind (unit: m s⁻¹, arrows). The white dots indicate that
 211 the composites with shading were above the 90% confidence level. The black boxes in (a) indicate the centers of the AC_{NC} and
 212 C_{PRD}, respectively. The green boxes in (b) and (c) represent the areas of NC and the PRD. Composites of the summer mass
 213 fluxes of O₃ (d) associated with the DP-O₃ (DP-O₃P minus DP-O₃N) for the area-averaged differences (NC minus PRD) from
 214 1980 to 2019. The bottom axis gives the names of the chemical and physical processes: chemical reaction (Chem), convection
 215 (Conv), PBL mixing (Mix), transport (Trans) and their sum (Sum).

216 Arctic SI in May was closely related to summer O₃ pollution in NC (Yin et al. 2019), but its effects on the
 217 north-south dipole distribution of O₃ had not been studied. The meridional O₃ dipole pattern in the east of China
 218 was positively correlated with SI anomalies near the Franz Josef Land (SI_{FJL}). Note that the correlation between
 219 them remains unchanged after the signal of El Niño-Southern Oscillation (ENSO) was removed. The area-
 220 averaged (82–88°N, 3°W–60°E; 79–88°N, 60–90°E; denoted by the green boxes in Fig. 4a) SI in May was
 221 calculated and defined as the SI_{FJL} index, whose linear correlation coefficient with the time series of DP-O₃ was
 222 0.52 (exceeding the 99% confidence level). When the SI_{FJL} anomalies were significant (i.e., |anomalies| > its one
 223 standard deviation), the occurrence probability of the DP-O₃ in the same phase was 83% (Fig. 2). Furthermore,
 224 the active centers of the anomalous atmospheric circulations and meteorological conditions associated with SI_{FJL}
 225 in the east of China were similar to that of the DP-O₃ (i.e., NC and PRD). That is, positive SI_{FJL} anomalies were
 226 conducive to less (more) precipitation, less (more) cloud cover, and strong (weak) solar radiation in NC (PRD)

227 (Fig. 4c, Fig. S4). The chemical and physical processes of ozone production in GEOS-Chem simulations were
 228 analyzed. The difference of chemical reactions between NC and PRD had a large positive value (11.6 Tons d⁻¹),
 229 and the difference of the sum of all chemical and physical processes was 7.0 Tons d⁻¹ (Fig. 4c), resulting in DP-
 230 O₃.



231
 232 **Figure 4** Composites of (a) May SI concentration and (b) JFM SST associated with the DP-O₃ (DP-O₃P minus DP-O₃N) from
 233 1980 to 2019. The green boxes in (a) and (b) indicate where the SI_{FJL} and SIOD indices are calculated, respectively. The white
 234 dots indicate that the composites were above the 90% confidence level. Composite summer meteorological conditions,
 235 circulations and mass fluxes of O₃ associated with (c) SI_{FJL} (positive SI_{FJL} years minus negative SI_{FJL} years) and (d) SIOD
 236 (positive SIOD years minus negative SIOD years) from 1980 to 2019. The bottom axis gives the names of the meteorological
 237 conditions and chemical and physical processes: the differences between AC_{NC} and C_{PRD} (unit: 10 gpm), surface incoming
 238 shortwave flux (Ssr, unit: W m⁻²), surface air temperature (SAT, unit: K), and precipitation (Prec, unit: mm); chemical reaction
 239 (Chem, unit: Tons d⁻¹), convection (Conv, unit: Tons d⁻¹), PBL mixing (Mix, unit: Tons d⁻¹), transport (Trans, unit: Tons d⁻¹)
 240 and their sum (Sum, unit: Tons d⁻¹).

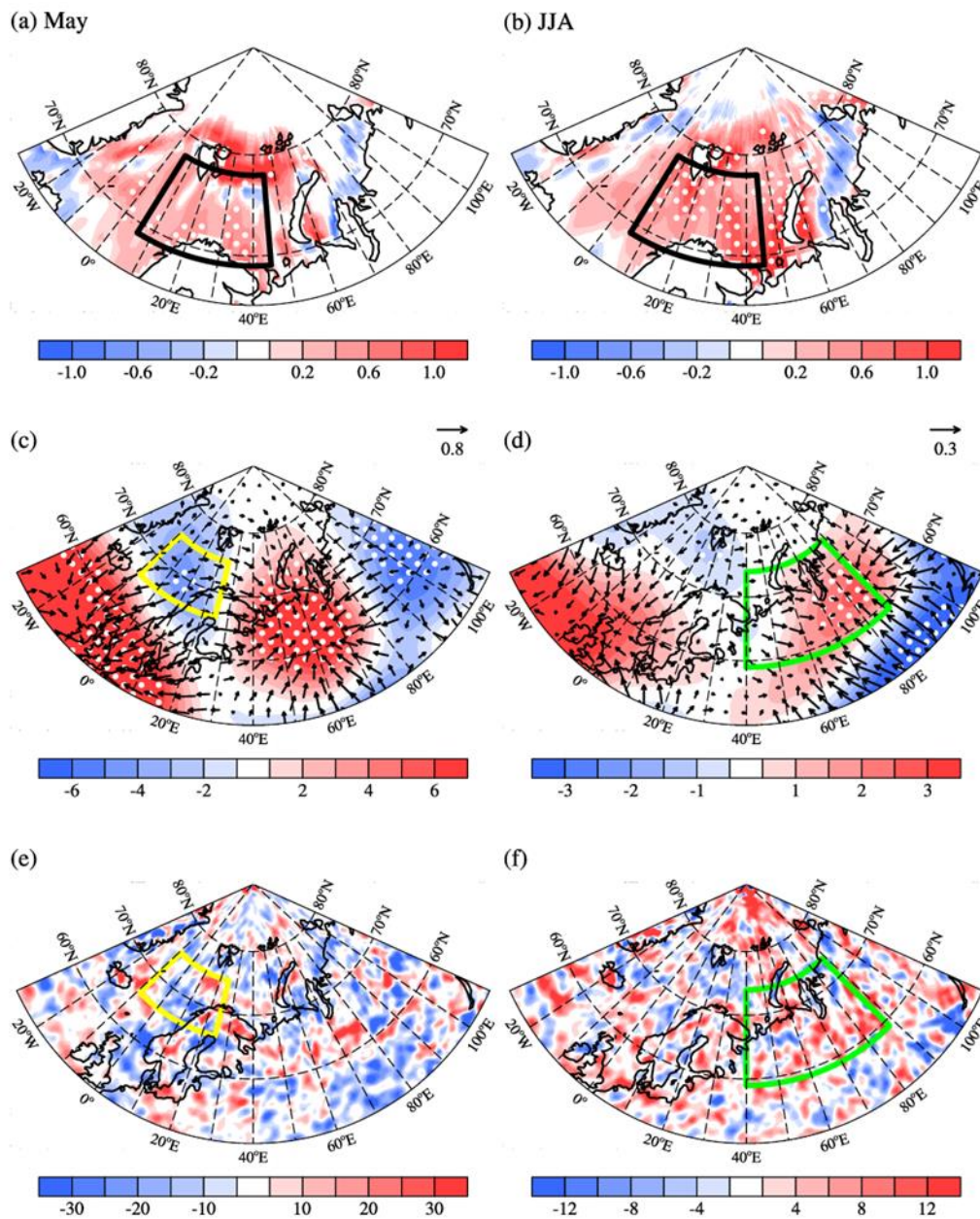
241 In addition to the signal from the Arctic, SST as an effective external forcing also has significant influences
 242 on summer climate in the east of China (Li et al. 2018). Therefore, it was important to answer the question whether
 243 SST could affect the DP-O₃ in the east of China in summer. Large anomalies of preceding January–February–
 244 March (JFM) SST over the southern Indian Ocean was obvious when we evaluated the relationship between the
 245 DP-O₃ and previous SST. After removing the influence of ENSO, the SST signal in the southern Indian Ocean
 246 still maintains (Fig. 4b). The two regions with significant anomalies were similar to the Subtropical Indian Ocean

247 Dipole (SIOD) regions found by Behera and Yamagata (2001). Variance analysis and correlation analysis of SST
248 in the Indian Ocean also indicated that a SST dipole type oscillation occurred in the southern Indian Ocean, which
249 usually developed in the preceding winter and reaches its strongest in the subsequent January to March (Jia and
250 Li 2013). The difference between the mean SST of the two regions (29–40°S, 31–62°E and 7–25°S, 55–86°E;
251 green box in Fig. 4b; the southwest positive pole minus the northeast negative pole) was defined as the SIOD
252 index and calculated (Fig. 2). The linear correlation coefficient between the SIOD index and the time series of
253 DP-O₃ from 1980 to 2019 was 0.44 (significant at the 99% confidence level). When the SIOD anomalies were
254 significant (i.e., |anomalies| > its one standard deviation), the occurrence probability of DP-O₃ in the same phase
255 is 82% (Fig. 2). Furthermore, the composite meteorological conditions in the positive and negative phases of
256 SIOD had similar centers to that of DP-O₃. That is, the anticyclone over NC was always accompanied by hot-dry
257 meteorological condition, while the cyclone over PRD was always accompanied by cool-moist environment (Fig.
258 4d; Fig. S5). The chemical reactions increased 12.3 Tons d⁻¹ in NC comparing to those in the PRD (Fig. 4 d),
259 indicating that the strong solar radiation and high temperature conditions actually enhanced the chemical reactions
260 in the atmosphere to produce more O₃ in NC.

261 **4. Associated physical mechanisms**

262 Changes in SI_{FJL} and SIOD both could possibly contribute to the formation of DP-O₃. Note that SI_{FJL} and
263 SIOD have few years of common significant anomalies, more than 78% of the individual sample years were used
264 to make composite with both indices. The correlation coefficient between them was only 0.21 and was not
265 significant, indicating that SI_{FJL} and SIOD were independent of each other. Several previous studies have
266 documented that the preceding Arctic SI anomalies could trigger EU-like atmospheric responses in the subsequent
267 summer, and thus influenced the climate in the east of China (Wang and He 2015). Corresponding to reduced
268 SI_{FJL}, SST anomalies in the Barents and Kara Sea were significantly positive and gradually increase from May to
269 summer months (Fig. 5a, b). The warm SST anomalies influenced local heat anomalies and caused anomalous
270 atmospheric circulations. Following the decrease in SI_{FJL}, anomalous divergent winds appeared in the mid-
271 troposphere, which were accompanied by warm SST anomalies and negative velocity potential anomalies (yellow
272 box in Fig. 5c). As proposed by Xu et al., (2021), the rotational component of the anomalous divergent winds
273 could spread to the south and force the vorticity generation over Eurasia. Thus, during the subsequent summer,
274 significant convergence and positive velocity potential with a positive Rossby wave source anomaly occurred over
275 northern Europe and West Siberia (green box in Fig. 5d). We also used the SST anomalies associated with SI_{FJL}
276 (in Barents and Kara Sea in JJA) to composite relevant variables. Significant convergence, positive velocity

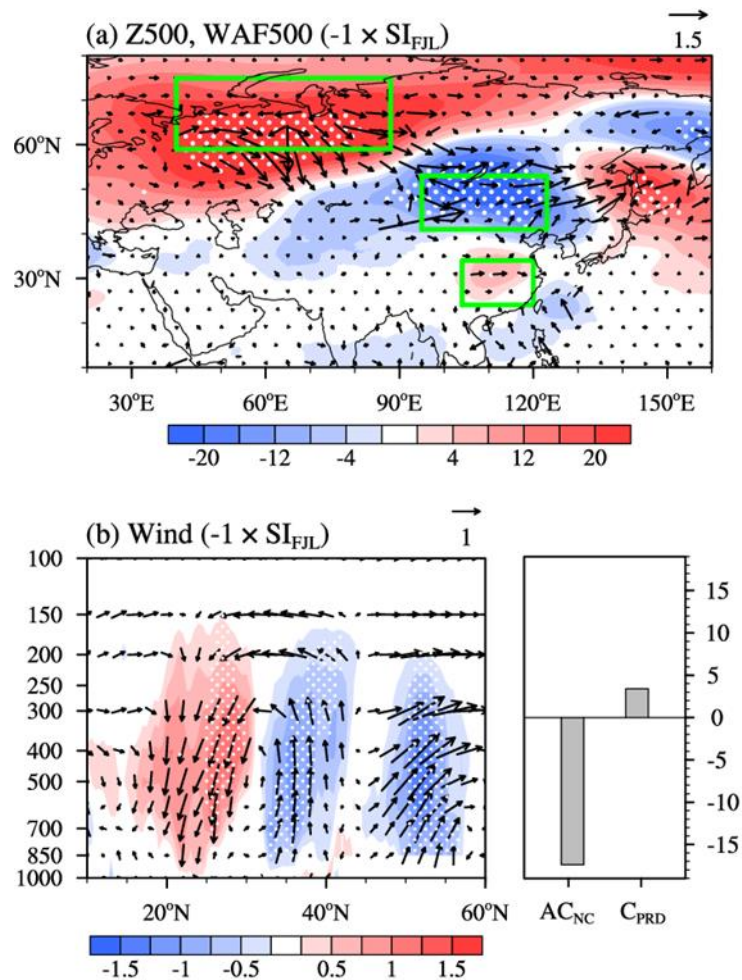
277 potential, and positive Rossby source anomaly all appeared over Europe and West Siberia in JJA (Fig. S6). This
 278 indicated that positive anomalies of Rossby-wave source over Europe and West Siberia could be generated
 279 by local heat anomalies associated with decreased SI_{FJL} in the Barents and Kara Sea.



280
 281 **Figure 5** Composites of (a) May Arctic SST (unit: K), (c) velocity potential (unit: $10^5 \text{ m}^2 \text{ s}^{-1}$, shading) and divergent wind at
 282 500 hPa (unit: m s^{-1} , arrows), and (e) Rossby wave source anomalies at 500 hPa (unit: 10^{-11} s^{-2}) associated with SI_{FJL} index
 283 (negative SI_{FJL} years minus positive SI_{FJL} years) from 1980 to 2019. The back box in (a) and (b), yellow box in (c) and (e) and
 284 green box in (d) and (f) represents the center of the SST, velocity potential and Rossby wave source anomaly associated with
 285 SI_{FJL} , respectively. The white dots indicate that the composites with shading were above the 90% confidence level.

286 Moreover, corresponding to the decreased SI_{FJL} , the anomalous Rossby WAF propagated from Europe and
 287 West Siberia (consistent with the aforementioned Rossby wave source) to Northeast China and enhanced the
 288 cyclonic anomaly nearby (Fig. 6a). The anomalous cyclonic circulation caused ascending motion from the surface

289 up to 300 hPa over NC, and further induced a meridional circulation with an anomalous descending branch near
 290 20°N (Fig. 6b). Likewise, an anomalous anticyclone occurred in the middle troposphere above the PRD (Fig.
 291 6b). In other words, an EU-like Rossby wave train was induced in the mid-troposphere (Fig. 6a), which
 292 propagated from northern Europe and West Siberian Plain (+), reaching the broad area from northeastern China
 293 (-) to the south of China (+). Thus, the reduction in SI near the Franz Josef Land in the May modulated the EU-
 294 like pattern in the subsequent summer and strengthened the anomalous cyclonic and anticyclonic circulations over
 295 NC and the PRD (Fig. 6b), respectively. The differences in anomalous atmospheric circulations and associated
 296 meteorological conditions between NC and the PRD make great contributions to the occurrence of DP-O₃.

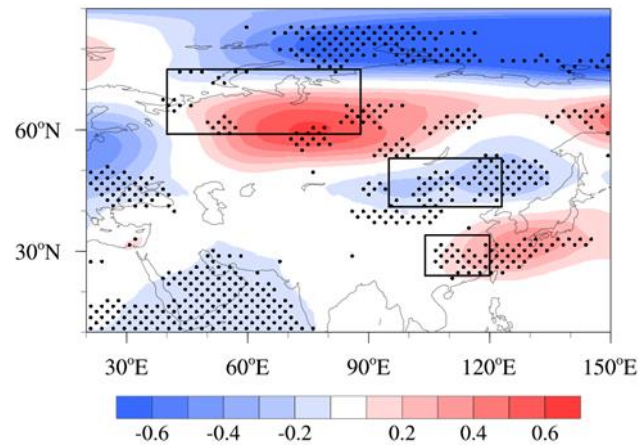


297

298 **Figure 6** Composites of (a) wave activity flux anomalies (unit: $\text{m}^2 \text{s}^{-2}$, arrows), geopotential height (unit: gpm, shading) at 500
 299 hPa and (b) mean wind (unit: m s^{-1} , arrows), omega (unit: $10^{-2} \text{ Pa s}^{-1}$, shading) over 100–130° E, and the anomalies of AC_{NC}
 300 and C_{PRD} (unit: gpm, bar) in summer associated with SI_{FJL} index (negative SI_{FJL} years minus positive SI_{FJL} years) from 1980
 301 to 2019. The green boxes in (a) represent the centers of the EU-like pattern. The white dots indicate that the composites with
 302 shading were above the 90% confidence level.

303 The relationship between the preceding May SI anomalies and the JJA EU-like pattern was also confirmed
 304 by large ensemble simulations of CESM during 1980–2019. According to the simulated sea ice fraction near the
 305 Franz Josef Land, the three years with the lowest and highest SI in each member were selected to construct the

306 composite maps based on all the 40 available members. The difference in JJA geopotential height at 500 hPa
 307 represented the atmospheric response to declining May SI_{FJL} . As shown in Fig. 7, the decline of SI_{FJL} in May led
 308 to an EU-like pattern in the subsequent summer over Eurasia, which was in good accordance with the observed
 309 result (Fig. 6a). The anticyclonic and cyclonic anomalies shown in the geopotential height at 500 hPa (i.e., AC_{NC}
 310 and C_{PRD}) in summer were also well reproduced by over 60% of the members. The above results confirmed the
 311 robustness of the physical mechanisms proposed in the present study.

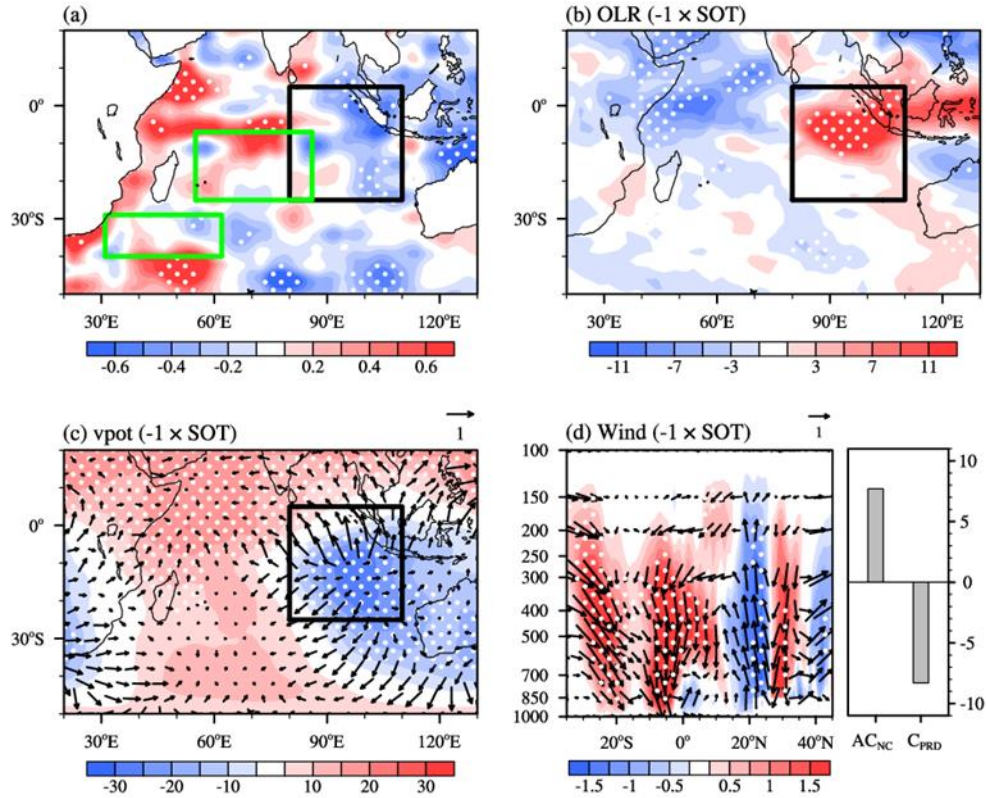


312

313 **Figure 7** Composite differences of geopotential height at 500 hPa in JJA between three low and high SI_{FJL} years based on the
 314 ensemble of 40 CESM-LE simulations during 1980–2019. The black dots indicate that the mathematical sign of the composite
 315 results of more than 60 % of the members is consistent with the ensemble mean. The black boxes represent the centers of the
 316 EU-like pattern.

317 SIOD could influence atmospheric anomalies and distribution of summer precipitation in China mainly
 318 through Hadley circulation (Liu et al. 2019). Can SIOD anomalies also influenced the DP- O_3 via meridional
 319 atmospheric forcing? Despite the significant correlation between SIOD anomalies (defined by SST) and the DP-
 320 O_3 in the east of China (Fig. 4b), it should be noted that the thermodynamic signals in the southern Indian Ocean
 321 not only existed on the sea surface but also extended to the subsurface (Fig. S7). As time goes by, the center of
 322 negative SST anomalies moved to the northeast possibly due to the eastward movement of atmospheric forcing
 323 caused by the mean westerly flow (Behera and Yamagata 2001). When it moved to the vicinity of Sumatra Island
 324 in JJA, the abnormally cold signals of SST could extend downward from the surface to 60m (black box in Fig.
 325 8a). The area-averaged (black box in Fig. 8a) summer-mean subsurface ocean temperature of 0–60m was defined
 326 as the SOT index and calculated. Affected by negative SOT anomalies near Sumatra Island, the equatorial eastern
 327 Indian Ocean convection was suppressed (indicated by positive anomalies of OLR in Fig. 8b) and significant
 328 divergence prevailed in the lower troposphere (Fig. 8c). As a result, anomalous downward air flow developed near
 329 Sumatra Island from 300 hPa to the surface (about 20–5°S in Fig. 8d). This anomalous downward air flow
 330 modulated the meridional circulation over 90–120 °E by strengthening the abnormal upward airflow at 20°N and

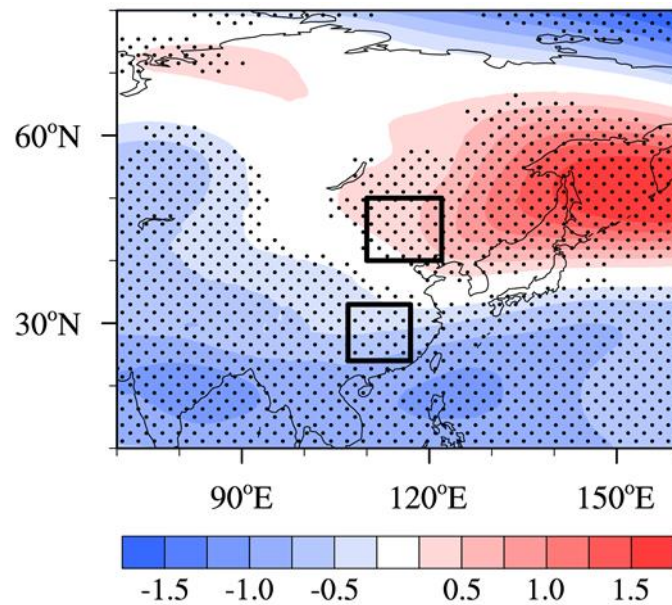
331 downward airflow at 30°N. Thus, the AC_{NC} and C_{PRD} were enhanced simultaneously (Fig. 8d). Overall, following
 332 the positive phase of SIOD, the cold signal of SOT anomalies changed the meridional circulation in the subsequent
 333 JJA and strengthened the C_{PRD} and AC_{NC} in the troposphere above the east of China. Under these large-scale
 334 atmospheric anomalies, O_3 concentrations became higher in NC, whereas the generation of surface O_3 were
 335 weakened in the PRD.



336
 337 **Figure 8** (a) Composites of mean 0–60m subsurface ocean temperature (unit: K) in summer associated with the SIOD (positive
 338 SIOD years minus negative SIOD years) from 1980 to 2019. The green boxes represent the centers of the SIOD, and the black
 339 box indicates where the SOT index is calculated. Composites of (b) OLR (unit: $W m^{-2}$) and (c) velocity potential (unit: $10^5 m^2$
 340 s^{-1} , shadings) and divergent winds (unit: $m s^{-1}$, vectors) at 10 m in summer associated with SOT indexes of opposite sign
 341 (negative SOT years minus positive SOT years). The black box represents the center of the SOT. (d) Composites of summer
 342 mean winds (unit: $m s^{-1}$, arrows) and omega (unit: $10^{-2} Pa s^{-1}$, shadings) over 90–120°E, and the anomalies of AC_{NC} and C_{PRD}
 343 (unit: gpm, bars) associated with SOT indexes of opposite sign. The white dots indicate that the composites with shading were
 344 above the 90% confidence level.

345 The CESM-LE datasets were also used to verify the statistical correlation between the preceding SIOD and
 346 large-scale atmospheric circulations in JJA. The composite differences of SIOD in JFM between the three high
 347 years and three low years of SST simulated by each ensemble member during 1980–2019 were investigated based
 348 on the ensemble of 40 CESM-LE simulations. The composite results (positive SIOD years minus negative SIOD
 349 years) of atmospheric circulations could be considered as the relevant atmospheric circulation responses
 350 associated with differences in SIOD. More than 60% of the CESM ensemble members could well reproduce the

351 anticyclonic circulation over NC and the cyclonic circulation over the PRD in summer at 500hPa (Fig. 9). That is,
 352 the CESM-LE also confirmed the relationship between the previous JFM SIOD anomaly and the DP-O₃-related
 353 atmospheric circulations (i.e., AC_{NC} and C_{PRD}) in subsequent JJA.



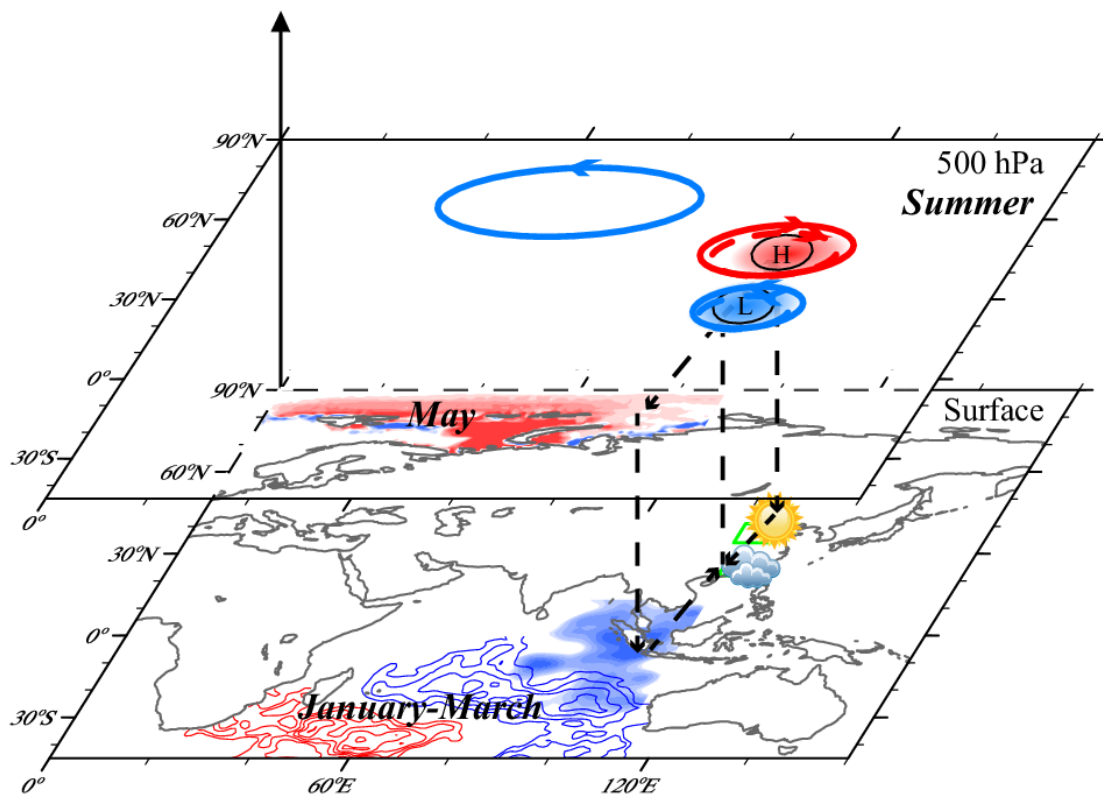
354
 355 **Figure 9** Composite differences of geopotential height at 500 hPa in JJA between three high and low SIOD years based on the
 356 ensemble of 40 CESM-LE simulations during 1980–2019. The black dots indicate that the mathematical sign of the composite
 357 results of more than 60 % of the members is consistent with the ensemble mean. The black boxes represent the centers of AC_{NC}
 358 and C_{PRD}, respectively.

359 5. Conclusions and discussions

360 In general, the O₃ concentrations in NC were substantially high and the problem of O₃ pollution in the PRD
 361 has become increasingly prominent in recent years. A south-north dipole pattern of O₃ concentration in the east of
 362 China was identified based on GEOS-Chem simulations with fixed emissions and changing meteorological
 363 condition from 1980 to 2019. The DP-O₃ pattern presented opposite centers in NC and PRD. Corresponding to
 364 the positive phase of DP-O₃, cyclonic and anticyclonic anomalies were located over the PRD and NC respectively,
 365 which resulted in dry and hot climate in NC, while the environment in the PRD region was cool and moist. The
 366 opposite was true in the negative phase of DP-O₃. During positive phases, the meteorological condition mentioned
 367 above significantly enhanced photochemical reactions in NC but suppressed O₃ production in the PRD, and thus
 368 make great contributions to the south-north dipole pattern of O₃ in the east of China.

369 Arctic SI near the Franz Josef Land in May played an important role in the occurrence of DP-O₃. The warm
 370 SST anomalies associated with less SI_{FIL} could induce divergent wind field and vorticity advection in the upper
 371 layer, and enhanced positive Rossby wave source over northern Europe and West Siberia in summer. An EU-like

372 pattern was triggered in Eurasia (solid lines in Fig. 10), which could enhance the DP-O₃-related atmospheric
 373 circulation (i.e., AC_{NC} and C_{PRD}) in JJA. As a result, meteorological conditions for O₃ concentration were
 374 completely different between NC and PRD, which eventually contributed the formation of DP-O₃. In addition, the
 375 precursory climatic driving signal of SIOD anomalies in the low latitudes in JFM was also closely linked to DP-
 376 O₃. The thermodynamic signal of SIOD could be stored in the subsurface, and the center of negative SST
 377 anomalies moved to the vicinity of Sumatra Island in summer. The meridional circulation intensified in summer
 378 (dashed lines in Fig. 10), which, along with the enhancement of the AC_{NC} and C_{PRD} over the east of China,
 379 effectively increased O₃ concentration in NC but suppressed the generation of surface O₃ in the PRD. The linkages
 380 and corresponding physical mechanisms were well reproduced by the large CESM-LE ensemble simulation.



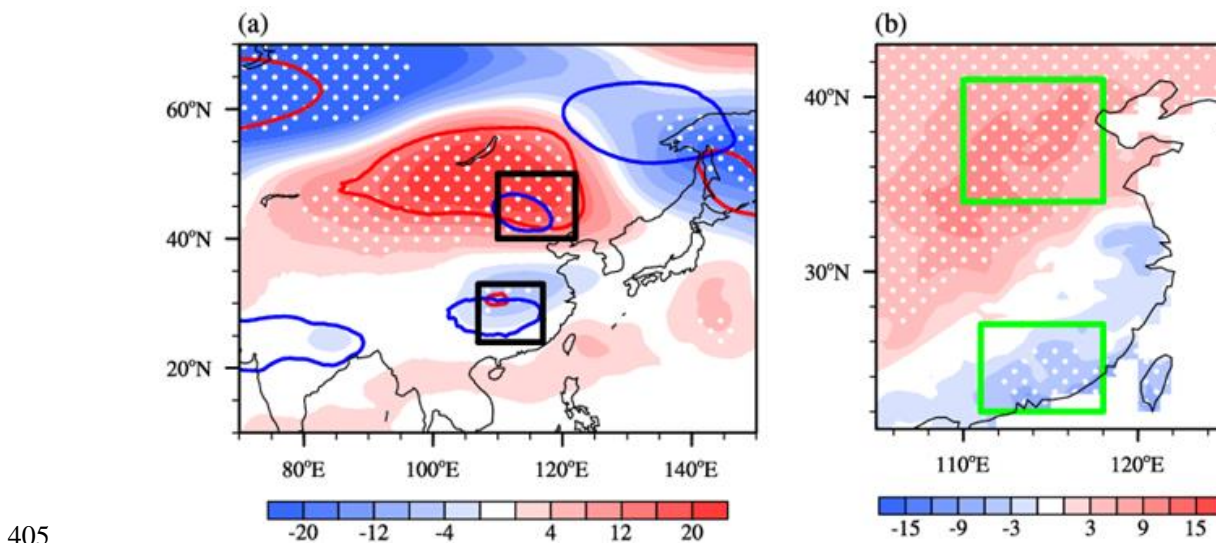
381
 382 **Figure 10** Schematic diagrams of the associated physical mechanisms. The May SI anomalies near the Franz Josef Land (red
 383 shadings) could trigger an EU-like pattern in the atmosphere in summer, which enhances the anticyclonic anomaly over NC
 384 and the cyclonic anomaly over the PRD. The thermodynamic signal of the preceding SIOD (contours) could be stored in the
 385 subsurface and the center of negative SST anomalies moves to the vicinity of Sumatra Island in summer (blue shading). The
 386 meridional circulation was enhanced in summer (dashed lines), along with the enhancement of AC_{NC} and C_{PRD} over eastern
 387 China. The solid lines indicate the anomalous atmospheric circulations affected by SI_{FJL}, while the dashed lines indicate the
 388 anomalous atmospheric circulations affected by SIOD.

389 The above analysis has revealed that the DP-O₃ is independently affected by SIOD and SI_{FJL} from 1980 to
 390 2019. We attempted to discuss the combined impacts of the two precursory climatic drivers in the present
 391 study. For this purpose, a synthetic climate variability index SEI, defined as the weighted average of SI_{FJL} and

392 SIOD, is calculated by

393
$$SEI = \frac{r_1 \times SI_{FJL} + r_2 \times SIOD}{|r_1| + |r_2|}$$

394 where r_1 and r_2 were the correlation coefficients of SI_{FJL} ($r_1 = 0.52$) and SIOD ($r_2 = 0.44$) with the DP- O_3
395 time series, respectively. The correlation coefficient between SEI and DP- O_3 was 0.62 (Fig. 2, exceeding the
396 99% confidence level). When the SEI anomalies were significant, the occurrence probability of the DP- O_3 in the
397 same phase was 93% (Fig. 2), which is higher than that based on individual influences of the two factors.
398 Composite atmospheric circulation analysis has been carried out based on years of positive and negative SEI
399 anomalies, and the results are shown in Fig. 11a. The composite atmospheric circulation based on the SEI index
400 was stronger, resulting in the concentrations of MDA8 O_3 in NC was $11.74 \mu\text{g m}^{-3}$ higher than that in PRD (Fig.
401 11b). The main areas influenced by SI and SST were slightly different. Although the two precursory climatic
402 drivers both could affect the atmospheric circulations over NC and the PRD, SI_{FJL} mainly affected atmospheric
403 circulation anomaly over NC, while SIOD played a major role in the PRD. However, climate variabilities at
404 different latitudes jointly facilitated the dipole pattern of O_3 in the east of China from 1980 to 2019.



406 **Figure 11** (a) Composites of geopotential height at 500 hPa (unit: gpm, shadings) in summer associated with the SEI (positive
407 SEI years minus negative SEI years) from 1980 to 2019. The red and blue lines indicate areas where the composite
408 geopotential height anomalies associated with SI_{FJL} and SIOD exceed the 90% confidence level, respectively. The black boxes
409 represent the centers of AC_{NC} and C_{PRD} , respectively. (b) Composite differences of the detrended summer-mean MDA8 O_3
410 (unit: $\mu\text{g m}^{-3}$) simulated by GEOS-Chem model between high and low SEI years during 1980–2019. The white dots indicate
411 that the composite differences are above the 90% confidence level. The green boxes represent the areas of NC and the PRD.

412 The north-south dipole pattern of O_3 in the east of China in summer and its relationship with climate factors
413 were clearly revealed in this study, yet some questions still remain unanswered and should be investigated in the
414 future. The GEOS-Chem model simulations were used to explore the dominant pattern of O_3 in the east of China

415 in summer due to the short sequence of O₃ observations. Although the GEOS-Chem demonstrated a good
416 performance based on evaluation, there still exist some differences between the simulations and observations. In
417 addition, statistical and numerical methods were used to reveal and verify the physical mechanisms behind the
418 dipole pattern of O₃ in the east of China and its relation with climate variability. However, further numerical
419 experiments should be carried out in the future. For example, coupled climate-chemistry models should be used
420 to not only simulated the influence of climate driving factors on O₃ pattern, but also revealed the effect of
421 individual climate factors as well as their comprehensive effects.

422

423 **Data Availability.**

424 Hourly O₃ concentration data could be downloaded from <https://quotsoft.net/air/> (Ministry of Environmental
425 Protection of China, 2020). Sea ice concentration, sea surface temperature, and subsurface ocean temperature data
426 were from <https://www.metoffice.gov.uk/hadobs/> (Met Office Hadley Centre, 2021). Monthly-mean MERRA-2
427 reanalysis dataset was available at <https://disc.gsfc.nasa.gov/datasets?page=1> (MERRA-2, 2021). The monthly
428 OLR data could be acquired from <http://olr.umd.edu/> (University of Maryland OLR Climate Data Record portal,
429 2021).

430

431 **Authors' contribution**

432 Yin Z. C. designed the research. Ma X. Q. did the statistical analysis and implemented the GEOS-Chem
433 simulations. Yin Z. C. and Ma X. Q. prepared the manuscript.

434

435 **Competing interests**

436 The authors declare that they have no conflict of interest.

437

438 **Acknowledgements**

439 This research was supported by National Natural Science Foundation of China (42025502, 42088101, 41991283)

440 and 91744311).

441

442

443

444 **References**

- 445 Behera, S. K., and Yamagata, T.: Subtropical SST dipole events in the southern Indian Ocean, *Geophys. Res. Lett.*,
446 28, 327–330, <https://doi.org/10.1029/2000GL011451>, 2001.
- 447 Bey, I., Jacob, D. J., Yantosca, R. M., Logan, J. A., Field, B., Fiore, A. M., Li, Q., Liu, H., Mickley, L. J., and
448 Schultz, M.: Global modeling of tropospheric chemistry with assimilated meteorology: Model description and
449 evaluation, *J. Geophys. Res.*, 106, 23073–23095, <https://doi.org/10.1029/2001JD000807>, 2001.
- 450 Chen, Z. Y., Zhuang, Y., Xie, X. M., Chen, D. L., Cheng, N. L., Yang, L., and Lia, R. Y.: Understanding long-
451 term variations of meteorological influences on ground ozone concentrations in Beijing During 2006–2016,
452 *Environ. Pollut.*, 245, 29–37, <https://doi.org/10.1016/j.envpol.2018.10.117>, 2019.
- 453 Gelaro, R., McCarty, W., Suarez, M. J., Todling, R., Molod, A., Takacs, L., Randles, C. A., Darmenov, A.,
454 Bosilovich, M. G., Reichle, R., Wargan, K., Coy, L., Cullather, R., Draper, C., Akella, S., Buchard, V., Conaty, A.,
455 da Silva, A. M., Gu, W., Kim, G. K., Koster, R., Lucchesi, R., Merkova, D., Nielsen, J. E., Partyka, G., Pawson, S.,
456 Putman, W., Rienecker, M., Schubert, S. D., Sienkiewicz, M., and Zhao, B.: The Modern-Era Retrospective Analysis
457 for Research and Applications, Version 2 (MERRA2), *J. Climate*, 30, 5419–5454, [https://doi.org/10.1175/jcli-d-](https://doi.org/10.1175/jcli-d-160758.1)
458 160758.1, 2017.
- 459 Good, S. A., Martin, M. J., and Rayner, N. A.: EN4: quality controlled ocean temperature and salinity profiles and
460 monthly objective analyses with uncertainty estimates, *J. Geophys. Res. Oceans*, 118, 6704–
461 6716, <https://doi.org/10.1002/2013JC009067>, 2013.
- 462 Han, H., Liu, J., Shu, L., Wang, T. J., and Yuan, H. L.: Local and synoptic meteorological influences on daily
463 variability in summertime surface ozone in eastern China, *Atmos. Chem. Phys.* 20, 203–222,
464 <https://doi.org/10.5194/acp-20-203-2020>, 2020.
- 465 Han, J. P., and Zhang, R. H.: The Dipole Mode of the Summer Rainfall over East China during 1958–2001, *Adv.*
466 *Atmos. Sci.*, 26, 727–735, <https://doi.org/10.1007/s00376-009-9014-6>, 2009.
- 467 Holtslag, A. and Boville, B. A.: Local versus nonlocal boundary layer diffusion in a global climate model, *J.*
468 *Climate*, 6, 1825–1842, [https://doi.org/10.1175/1520-0442\(1993\)006<1825:LVNBLD>2.0.CO;2](https://doi.org/10.1175/1520-0442(1993)006<1825:LVNBLD>2.0.CO;2), 1993.
- 469 Jia, X. L., and Li, C. Y.: Dipole oscillation in the Southern Indian Ocean and its impacts on climate, *Chinese J.*
470 *Geophys.*, 48, 1323–1335, <https://doi.org/10.1002/cjg2.780>, 2013.
- 471 Kay, J. E., Deser, C., Phillips, A., Mai, A., Hannay, C., Strand, G., Arblaster, J., Bates, S., Danabasoglu, G.,
472 Edwards, J., Holland, M., Kushner, P., Lamarque, J.-F., Lawrence, D., Lindsay, K., Middleton, A., Munoz, E.,
473 Neale, R., Oleson, K., Polvani, L., and Vertenstein, M.: The Community Earth System Model (CESM) Large
474 Ensemble Project: A community resource for studying climate change in the presence of internal climate
475 variability, *B. Am. Meteorol. Soc.*, 96, 1333–1349, <https://doi.org/10.1175/BAMS-D-13-00255.1>, 2015.
- 476 Li, H. X., Sun, B., Zhou, B. T., Wang, S. Z., Zhu, B. Y., and Fan, Y.: Effect of the Barents Sea ice in March on the
477 dipole pattern of air temperature in August in eastern China and the corresponding physical mechanisms, *Trans*
478 *Atmos Sci*, 44, 89–103, <https://doi.org/10.13878/j.cnki.dgkxxb.20130427001>, 2021.

479 Li, K., Jacob, D.J., Liao, H., Zhu, J., Shah, V., Shen, L., Bates, K. H., Zhang, Q., and Zhai, S. X.: A two-pollutant
480 strategy for improving ozone and particulate matter air quality in China, *Nat. Geosci.*, 12, 906–910,
481 <https://doi.org/10.1038/s41561-019-0464-x>, 2019.

482 Li, S. P., Wei, H., and Feng, G. L.: Atmospheric Circulation Patterns over East Asia and Their Connection with
483 Summer Precipitation and Surface Air Temperature in Eastern China during 1961–2013, *J Meteorol Res*, 32, 203–
484 218, <https://doi.org/10.1007/s13351-018-7071-4>, 2018.

485 Li, Z. Q., and Xiao, Z. N.: Thermal contrast between the Tibetan Plateau and tropical Indian Ocean and its
486 relationship to the South Asian summer monsoon, *Atmos Ocean Sci Lett*, 14, 100002,
487 <https://doi.org/10.1016/j.aosl.2020.100002>, 2021.

488 Liao, H., Chen, W. T., and Seinfeld, J. H.: Role of climate change in global predictions of future tropospheric
489 ozone and aerosols, *J. Geophys. Res.-Atmos.*, 111, D12304, <https://doi.org/10.1029/2005JD006852>, 2006.

490 Liu, H. L., Zhang, M. G., and Han, X.: A review of surface ozone source apportionment in China, *Atmos Ocean*
491 *Sci Lett*, 13, 470–484, <https://doi.org/10.1080/16742834.2020.1768025>, 2020.

492 Liu, L., Guo, J. P., Chen, W., Wu, R. G., Wang, L., Gong, H. N., Liu, B., Chen, D. D., and Li, J.: Dominant
493 Interannual Covariations of the East Asian-Australian Land Precipitation during Boreal Winter, *J. Climate*, 32,
494 3279–3296, <https://doi.org/10.1175/JCLI-D-18-0477.1>, 2019.

495 Lin, Z. D., and Li, F.: Impact of interannual variations of spring sea ice in the Barents Sea on East Asian rainfall
496 in June, *Atmos Ocean Sci Lett*, 11, 275–281, <https://doi.org/10.1080/16742834.2018.1454249>, 2018.

497 Lu, X., Zhang, L., Chen, Y., Zhou, M., Zheng, B., Li, K., Liu, Y., Lin, J., Fu, T.-M., and Zhang, Q.: Exploring
498 2016–2017 surface ozone pollution over China: source contributions and meteorological influences, *Atmos. Chem.*
499 *Phys.*, 19, 8339–8361, <https://doi.org/10.5194/acp-19-8339-2019>, 2019.

500 MERRA-2: meteorological data, available at: <https://disc.gsfc.nasa.gov/datasets?page=1>, last access: 1 September
501 2021.

502 Met Office Hadley Centre: Sea ice concentration, sea surface temperature, and subsurface ocean temperature data,
503 available at: <https://www.metoffice.gov.uk/hadobs/>, last access: 4 March 2021.

504 Ministry of Environmental Protection of China: Hourly O₃ concentration data, available at: <https://quotsoft.net/air/>,
505 last access: 23 September 2020.

506 North, G. R., Bell, T. L., Cahalan, R. F., and Moeng, F. J.: Sampling errors in the estimation of empirical
507 orthogonal functions *Mon. Weather Rev.*, 110, 699–706, [https://doi.org/10.1175/1520-0493\(1982\)110<0699:SEITEO>2.0.CO;2](https://doi.org/10.1175/1520-0493(1982)110<0699:SEITEO>2.0.CO;2), 1982.

509 Pu, X., Wang, T. J., Huang, X., Melas, D., Zanis, P., Papanastasiou, D. K., and Poupkou, A.: Enhanced surface
510 ozone during the heat wave of 2013 in yangtze river delta region, china, *Sci. Total Environ.*, 603, 807–
511 816, <https://doi.org/10.1016/j.scitotenv.2017.03.056>, 2017.

512 Rayner, N. A., Parker, D. E., Horton, E. B., Folland, C. K., Alexander, L. V., Rowell, D. P., Kent, E. C., and Kaplan,
513 A.: Global analyses of sea surface temperature, sea ice, and night marine air temperature since the late nineteenth

514 century, *J. Geophys. Res.*, 108, 4407, <https://doi.org/10.1029/2002JD002670>, 2003.

515 Rider, C. F., and Carlsten, C.: Air pollution and DNA methylation: effects of exposure in humans, *Clin Epigenetics*,
516 11, 131, <https://doi.org/10.1186/s13148-019-0713-2>, 2019.

517 Sardeshmukh, P. D., and Hoskins, B. J.: The generation of global rotational flow by steady idealized tropical
518 divergence, *J. Atmos. Sci.*, 45, 1228-1251, [https://doi.org/10.1175/1520-0469\(1988\)045<1228:TGOGRF>2.0.CO;2](https://doi.org/10.1175/1520-0469(1988)045<1228:TGOGRF>2.0.CO;2), 1988.

520 Takaya, K., and Nakamura, H.: A Formulation of a Phase-Independent Wave-Activity Flux for Stationary and
521 Migratory Quasigeostrophic Eddies on a Zonally Varying Basic Flow, *J. Atmos. Sci.*, 58, 608-627,
522 [https://doi.org/10.1175/1520-0469\(2001\)058<0608:AFOAPI>2.0.CO;2](https://doi.org/10.1175/1520-0469(2001)058<0608:AFOAPI>2.0.CO;2), 2001.

523 Tian, B, and Fan, K.: Climate prediction of summer extreme precipitation frequency in the Yangtze River valley
524 based on sea surface temperature in the southern Indian Ocean and ice concentration in the Beaufort Sea, *Int. J.*
525 *Climatol.*, 40, 4117–4130, <https://doi.org/10.1002/joc.6446>, 2019.

526 University of Maryland OLR Climate Data Record portal: OLR data, available at: <http://olr.umd.edu/>, last access:
527 28 May 2021.

528 Wang, H, and He, S.: The North China/northeastern Asia severe summer drought in 2014, *J. Climate*, 28, 6667–
529 6681, <https://doi.org/10.1175/JCLI-D-15-0202.1>, 2015.

530 Wang, J, and Guo, Y.: Possible impacts of Barents Sea ice on the Eurasian atmospheric circulation and the rainfall
531 of East China in the beginning of summer, *Adv Atmos Sci*, 21, 662-674, <https://doi.org/10.1007/BF02915733>,
532 2004.

533 Xia, S. W., Yin, Z. C., and Wang, H. J.: Remote Impacts from Tropical Indian Ocean on January Haze Pollution
534 over the Yangtze River Delta, *Atmos Ocean Sci Lett*, 14, 100042, <https://doi.org/10.1016/j.aosl.2021.100042>,
535 2021.

536 Xu, H. W., Chen, H. P., and Wang, H. J.: Interannual variation in summer extreme precipitation over Southwestern
537 China and the possible associated mechanisms, *Int J Climatol.* 41, 3425–3438, <https://doi.org/10.1002/joc.7027>,
538 2021.

539 Xu, W. Y., Xu, X. B., Lin, M. Y., Lin, W. L., Tarasick, D., Tang, J., Ma, J. Z., and Zheng, X. D.: Long-term trends
540 of surface ozone and its influencing factors at the Mt Waliguan GAW station, China – Part 2: The roles of
541 anthropogenic emissions and climate variability, *Atmos. Chem. Phys.*, 18, 773–798, <https://doi.org/10.5194/acp-18-773-2018>, 2018.

543 Yang, Y., Liao, H., and Li, J.: Impacts of the East Asian summer monsoon on interannual variations of summertime
544 surface-layer ozone concentrations over China, *Atmos. Chem. Phys.*, 14, 6867–6879, <https://doi.org/10.5194/acp-14-6867-2014>, 2014.

546 Yin, Z. C., and Ma, X. Q.: Meteorological Conditions Contributed to Changes in Dominant Patterns of Summer
547 Ozone Pollution in Eastern China, *Environ. Res. Lett.*, 15, 124062, <https://doi.org/10.1088/1748-9326/abc915>,
548 2020.

549 Yin, Z. C., Wang, H. J., Li, Y. Y., Ma, X. H., and Zhang, X. Y.: Links of Climate Variability among Arctic sea ice,
550 Eurasia teleconnection pattern and summer surface ozone pollution in North China, *Atmos. Chem. Phys.*, 19,
551 3857–3871, <https://doi.org/10.5194/acp-19-3857-2019>, 2019.

552 Zhao, Z. J., and Wang, Y. X.: Influence of the west pacific subtropical high on surface ozone daily variability in
553 summertime over eastern China, *Atmos. Environ.*, 170, 197–204, <https://doi.org/10.1016/j.atmosenv.2017.09.024>,
554 2017.

555 Zhou, D. R., Ding, A. J., Mao, H. T., Fu, C. B., Wang, T., Chan, L. Y., Ding, K., Zhang, Y., Liu, J., Lu, A., and
556 Hao, N.: Impacts of the East Asian monsoon on lower tropospheric ozone over coastal South China, *Environ. Res.*
557 *Lett.*, 8, 044011, <https://doi.org/10.1088/1748-9326/8/4/044011>, 2013.

558 **Table and Figure captions**

559 **Figure 1** (a) Spatial distributions of observed (dots) and GEOS-Chem simulated (shading) summer-mean MDA8
560 O₃ (unit: $\mu\text{g m}^{-3}$) for the period 2015–2019. (b) The second EOF spatial pattern of simulated summer-mean MDA8
561 O₃ from 1980 to 2019. The simulated O₃ concentrations were produced by GEOS-Chem with fixed emissions but
562 changing meteorological conditions from 1980 to 2019. The green boxes represent the areas of NC and the PRD.

563 **Figure 2** Variations in standardized DP-O₃ time series (black), May SI near the Franz Josef Land (SI_{FJL}, red),
564 January–February–March mean Subtropical Indian Ocean Dipole (SIOD, blue), and SEI (green) from 1980 to
565 2019. SEI defined as the weighted average of SI_{FJL} and SIOD. The correlation coefficients of the DP-O₃ with SI_{FJL}
566 (red), SIOD (blue), and SEI (green) were shown in the figure.

567 **Figure 3** Composite summer atmospheric circulations associated with the DP-O₃ (DP-O₃P minus DP-O₃N) for
568 the period 1980 to 2019, including (a) surface air temperature (SAT, unit: K, shadings) and geopotential height at
569 500 hPa (unit: 10 gpm, contours), (b) surface incoming shortwave flux (Ssr, unit: W m^{-2} , shadings) and low and
570 medium cloud cover (Mlcc, unit: 1, contours), and (c) precipitation (Prec, unit: mm, shadings) and surface wind
571 (unit: m s^{-1} , arrows). The white dots indicate that the composites with shading were above the 90% confidence
572 level. The black boxes in (a) indicate the centers of the AC_{NC} and C_{PRD}, respectively. The green boxes in (b) and
573 (c) represent the areas of NC and the PRD. Composites of the summer mass fluxes of O₃ (d) associated with the
574 DP-O₃ (DP-O₃P minus DP-O₃N) for the area-averaged differences (NC minus PRD) from 1980 to 2019. The
575 bottom axis gives the names of the chemical and physical processes: chemical reaction (Chem), convection (Conv),
576 PBL mixing (Mix), transport (Trans) and their sum (Sum).

577 **Figure 4** Composites of (a) May SI concentration and (b) JFM SST associated with the DP-O₃ (DP-O₃P minus
578 DP-O₃N) from 1980 to 2019. The green boxes in (a) and (b) indicate where the SI_{FJL} and SIOD indices are
579 calculated, respectively. The white dots indicate that the composites were above the 90% confidence level.
580 Composite summer meteorological conditions, circulations and mass fluxes of O₃ associated with (c) SI_{FJL}
581 (positive SI_{FJL} years minus negative SI_{FJL} years) and (d) SIOD (positive SIOD years minus negative SIOD years)
582 from 1980 to 2019. The bottom axis gives the names of the meteorological conditions and chemical and physical
583 processes: the differences between AC_{NC} and C_{PRD} (unit: 10 gpm), surface incoming shortwave flux (Ssr, unit: W
584 m^{-2}), surface air temperature (SAT, unit: K), and precipitation (Prec, unit: mm); chemical reaction (Chem, unit:
585 Tons d^{-1}), convection (Conv, unit: Tons d^{-1}), PBL mixing (Mix, unit: Tons d^{-1}), transport (Trans, unit: Tons d^{-1})
586 and their sum (Sum, unit: Tons d^{-1}).

587 **Figure 5** Composites of (a) May Arctic SST (unit: K), (c) velocity potential (unit: $10^5 \text{ m}^2 \text{ s}^{-1}$, shading) and
588 divergent wind at 500 hPa (unit: m s^{-1} , arrows), and (e) Rossby wave source anomalies at 500 hPa (unit: 10^{-11} s^{-2})
589 associated with SI_{FJL} index (negative SI_{FJL} years minus positive SI_{FJL} years) from 1980 to 2019. The back box in
590 (a) and (b), yellow box in (c) and (e) and green box in (d) and (f) represents the center of the SST, velocity potential
591 and Rossby wave source anomaly associated with SI_{FJL} , respectively. The white dots indicate that the composites
592 with shading were above the 90% confidence level.

593 **Figure 6** Composites of (a) wave activity flux anomalies (unit: $\text{m}^2 \text{ s}^{-2}$, arrows), geopotential height (unit: gpm,
594 shading) at 500 hPa and (b) mean wind (unit: m s^{-1} , arrows), omega (unit: $10^{-2} \text{ Pa s}^{-1}$, shading) over $100\text{--}130^\circ \text{ E}$,
595 and the anomalies of AC_{NC} and C_{PRD} (unit: gpm, bar) in summer associated with SI_{FJL} index (negative SI_{FJL} years
596 minus positive SI_{FJL} years) from 1980 to 2019. The green boxes in (a) represent the centers of the EU-like pattern.
597 The white dots indicate that the composites with shading were above the 90% confidence level.

598 **Figure 7** Composite differences of geopotential height at 500 hPa in JJA between three low and high SI_{FJL} years
599 based on the ensemble of 40 CESM-LE simulations during 1980–2019. The black dots indicate that the
600 mathematical sign of the composite results of more than 60 % of the members is consistent with the ensemble
601 mean. The black boxes represent the centers of the EU-like pattern.

602 **Figure 8** (a) Composites of mean 0–60m subsurface ocean temperature (unit: K) in summer associated with the
603 SIOD (positive SIOD years minus negative SIOD years) from 1980 to 2019. The green boxes represent the centers
604 of the SIOD, and the black box indicates where the SOT index is calculated. Composites of (b) OLR (unit: W m^{-2})
605 and (c) velocity potential (unit: $10^5 \text{ m}^2 \text{ s}^{-1}$, shadings) and divergent winds (unit: m s^{-1} , vectors) at 10 m in summer
606 associated with SOT indexes of opposite sign (negative SOT years minus positive SOT years). The black box
607 represents the center of the SOT. (d) Composites of summer mean winds (unit: m s^{-1} , arrows) and omega (unit:
608 $10^{-2} \text{ Pa s}^{-1}$, shadings) over $90\text{--}120^\circ \text{ E}$, and the anomalies of AC_{NC} and C_{PRD} (unit: gpm, bars) associated with SOT
609 indexes of opposite sign. The white dots indicate that the composites with shading were above the 90% confidence
610 level.

611 **Figure 9** Composite differences of geopotential height at 500 hPa in JJA between three high and low SIOD years
612 based on the ensemble of 40 CESM-LE simulations during 1980–2019. The black dots indicate that the
613 mathematical sign of the composite results of more than 60 % of the members is consistent with the ensemble
614 mean. The black boxes represent the centers of AC_{NC} and C_{PRD} , respectively.

615 **Figure 10** Schematic diagrams of the associated physical mechanisms. The May SI anomalies near the Franz Josef
616 Land (red shadings) could trigger an EU-like pattern in the atmosphere in summer, which enhances the
617 anticyclonic anomaly over NC and the cyclonic anomaly over the PRD. The thermodynamic signal of the
618 preceding SIOD (contours) could be stored in the subsurface and the center of negative SST anomalies moves to
619 the vicinity of Sumatra Island in summer (blue shading). The meridional circulation was enhanced in summer
620 (dashed lines), along with the enhancement of AC_{NC} and C_{PRD} over eastern China. The solid lines indicate the
621 anomalous atmospheric circulations affected by SI_{FJL} , while the dashed lines indicate the anomalous atmospheric
622 circulations affected by SIOD.

623 **Figure 11** (a) Composites of geopotential height at 500 hPa (unit: gpm, shadings) in summer associated with the
624 SEI (positive SEI years minus negative SEI years) from 1980 to 2019. The red and blue lines indicate areas where

625 the composite geopotential height anomalies associated with SI_{FJL} and SIOD exceed the 90% confidence level,
626 respectively. The black boxes represent the centers of AC_{NC} and C_{PRD} , respectively. (b) Composite differences of
627 the detrended summer-mean MDA8 O_3 (unit: $\mu g\ m^{-3}$) simulated by GEOS-Chem model between high and low
628 SEI years during 1980–2019. The white dots indicate that the composite differences are above the 90% confidence
629 level. The green boxes represent the areas of NC and the PRD.

630